

# Large-Eddy Simulation of the Flow Over a Circular Cylinder at Reynolds Number 3900 Using the OpenFOAM Toolbox

Dmitry A. Lysenko · Ivar S. Ertesvåg · Kjell Erik Rian

Received: 20 September 2011 / Accepted: 11 July 2012 / Published online: 3 August 2012  
© Springer Science+Business Media B.V. 2012

**Abstract** The flow over a circular cylinder at Reynolds number 3900 and Mach number 0.2 was predicted numerically using the technique of large-eddy simulation. The computations were carried out with an O-type curvilinear grid of size of  $300 \times 300 \times 64$ . The numerical simulations were performed using a second-order finite-volume method with central-difference schemes for the approximation of convective terms. A conventional Smagorinsky and a dynamic  $k$ -equation eddy viscosity sub-grid scale models were applied. The integration time interval for data sampling was extended up to 150 vortex shedding periods for the purpose of obtaining a fully converged mean flow field. The present numerical results were found to be in good agreement with existing experimental data and previously obtained large-eddy simulation results. This gives an indication on the adequacy and accuracy of the selected large-eddy simulation technique implemented in the OpenFOAM toolbox.

**Keywords** Large-eddy simulation · Conventional Smagorinsky SGS model · Dynamic  $k$ -equation SGS model · Finite-volume method · Turbulent separated flow · Circular cylinder

## 1 Introduction

The long-term goal of the present work is to develop a large-eddy simulation (LES) model for high Reynolds number flows of practical interest with further adaptation for turbulent combustion modeling. The core numerical method is based on the

---

D. A. Lysenko (✉) · I. S. Ertesvåg  
Department of Energy and Process Engineering,  
Norwegian University of Science and Technology,  
Kolbjørn Hejes vei 1B, Trondheim 7491, Norway  
e-mail: dmitry.lysenko@ntnu.no

K. E. Rian  
Computational Industry Technologies AS, Trondheim 7462, Norway

OpenFOAM toolbox which was originally developed as an high-end C++ classes library (Field Operation and Manipulation) for a broad range of fluid dynamics applications, but quickly became very popular in industrial engineering as well as in academic research (for example, there are at least two annual international conferences dedicated to the library development and evaluation). The basic numerical approach for Navier-Stokes equations solution is based on the so-called projection procedure [5] in the frame of the factorized finite-volume method (FVM). The long list of numerical schemes and mathematical models implemented in OpenFOAM provides robustness and efficiency for a wide spectrum of fluid dynamics problems.

Nevertheless, in spite of many attractive features, OpenFOAM has some disadvantages, as well. The most crucial among them are: (1) the absolute lack of default settings; (2) the huge amount of different numerical schemes and models (which is an advantage for the expert users); (3) the absence of a quality certification following from a lack of high-quality documentation and references. Thus, the problem of validation and verification of OpenFOAM capabilities becomes more principal and fundamental compared to other, commercial CFD codes.

Previously, a methodical investigation for several plane turbulent bluff-body flows has been carried out with the goal of validation, verification and understanding of the numerical method capabilities implemented in OpenFOAM using the conventional compressible URANS approach [22–24]. These results were analyzed in detail and agreed fairly well with experimental data. Based on the optimistic results, the numerical method was extended to a large-eddy simulation model. The main objective was to evaluate the applicability of the implemented LES approach for predictions of turbulent separated flows. In the present study, we have performed a validation of the LES technique for a sub-critical circular cylinder flow at the Reynolds number  $Re = \rho_\infty U_\infty D / \mu = 3900$  (where  $U_\infty$  and  $\rho_\infty$  are the free-stream velocity and mass density, respectively,  $D$  is the diameter of the circular cylinder and  $\mu$  represents the dynamic viscosity). The simulation was done for a Mach number of  $M = U_\infty / c_\infty = 0.2$  (where  $c_\infty$  is the speed of sound in the free stream).

### 1.1 Experimental and direct numerical simulation references

The turbulent flow over a circular cylinder at  $Re = 3900$  is well documented in the literature and can be viewed as a generic benchmark for the sub-critical regime [35]. Available experimental data for this particular test case cover the most important integral (such as forces, wake dynamics, separation angle and recirculation bubble) and local (velocity, vorticity and Reynolds stresses) features of the flow allowing to assess a numerical method qualitatively and quantitatively. In spite of some experimental difficulties (the presence of the recirculation zone and high instantaneous flow angles), there are several hot-wire anemometry (HWA) and particle image velocimetry (PIV) measurements available in the near wake of the circular cylinder. Other experimental data for mean pressure and vorticity are also available. For example, Norberg [31] provided pressure measurements at the surface of a cylinder, and Son and Hanratty [40] obtained mean vorticity at the surface of a cylinder for  $Re = 5000$ .

Pioneering work was done by Ong and Wallace [33], who managed to accurately measure velocity and vorticity vectors in the near wake outside the recirculation bubble and proposed turbulence statistics and power spectra of the stream-wise

and normal velocity components at several locations. To avoid the restrictions associated with the presence of back flow, the techniques of particle image (PIV) or laser Doppler (LDV) velocimetry are more appropriate [35]. One of the first PIV works for the flow over a circular cylinder at  $Re = 3900$  was the study of Lourenco and Shih [21], who performed time resolved measurements in the recirculation region. Statistical quantities were assessed even though this PIV experiment was not designed for this purpose. Nevertheless, these results are often used as reference for validation of the numerical simulations in the literature (e.g. Beaudan and Moin [2], Mittal and Moin [30], Breuer [3]).

Dong et al. [6] investigated the near wake with PIV and direct numerical simulation (DNS) at Reynolds numbers of 3900, 4000 and 10000. The main emphasis was put on an investigation of the shear-layer instability using DNS data, but a PIV/DNS comparison of mean and turbulent isocontours PIV/DNS maps was also discussed. Recently, the flow over a circular cylinder was studied by Parnaudeau et al. [35] in the near wake at  $Re = 3900$  both numerically (LES) and experimentally with PIV and HWA methods. However, the PIV data of Parnaudeau et al. [35] differed from those of Lourenco and Shih [21], but were at the same time consistent with HWA data of Ong and Wallace [33], and as pointed out by Meyer et al. [28], were inconsistent with their own hot-wire data. Wissink and Rodi [44] performed a series of DNS at  $Re = 3300$  with different span-wise sizes of the computational domain. The results of Wissink and Rodi were found to be in a good agreement with experimental data obtained for  $Re = 3900$  taking an offset in the stream-wise direction into account.

## 1.2 LES references

Many large-eddy simulations have been conducted for the flow over a circular cylinder at  $Re = 3900$  during the past two decades. Beaudan and Moin [2] were the first to perform a numerical analysis using LES for this test case. In this paper we have tried to collect and summarize the most referenced LES studies in the literature for this particular case. The main attention was put on the computational domain, grid type, grid resolution and numerical method (Table 1). The following symbols and abbreviations are used: T—grid type (O, C, H, O-H, UN—unstructured);  $L_x$ ,  $L_y$ ,  $L_z$ —spatial dimension of a computational domain in stream-wise ( $x$ ), transverse ( $y$ ) and span-wise ( $z$ ) coordinates (Fig. 1); S—grid size; MT—solution method for the filtered Navier-Stokes equations (FDM—finite-difference method, HOFDM—high order FDM, FVM—finite-volume method, FEM—finite-element method); SD—spatial discretization (CDS—central differencing, GB—Galerkin B-spline, MUSCL—monotone upwind scheme for conservation laws); TD—time discretization (FS—fractional step, RK—Runge-Kutta, AB—Adams-Bashforth, BDF—backward); SGS—sub-grid scale model (DSM—dynamic Smagorinsky, DKE—dynamic  $k$ -equation, SF—structure function, MILES—monotone integrated LES, ILES—implicit LES, WALE—wall-adaptive eddy viscosity).

Here are some observations: The most popular mesh type is O-type or C-type. Only a few calculations [28, 35, 45] have been carried out using structured H-type and unstructured (with rectangular computational domain) grids. As was reported by several researchers (e.g. [31, 35]), both from experimental and numerical points of view, the aspect ratio (hereafter AR) may be considered as the most important factor, that have significant impact on the main flow parameters (especially on

**Table 1** LES of the circular cylinder flow at  $Re = 3900$ : numerical aspects

Contributors	T	$L_x$	$L_y$	$L_z$	S	MT	SD	TD	SGS
Mittal and Moin [30]	C	$36 \times D$	$50 \times D$	$\pi \times D$	$401 \times 120 \times 48$	FVM	CDS-2	FS-2	DSM
Breuer, Case D3 [3]	O	$30 \times D$	$30 \times D$	$\pi \times D$	$165 \times 165 \times 64$	FVM	CDS-2	RK-2	DSM
Kravchenko and Moin [19]	O	$60 \times D$	$60 \times D$	$2\pi \times D$	$205 \times 185 \times 48$	HOFDM	GB	RK-3	DSM
Franke and Frank [7]	O	$30 \times D$	$20 \times D$	$\pi \times D$	$185 \times 193 \times 33$	FVM	CDS-2	RK-3	DKE
Alkishiwi et al. [1]	C	$25 \times D$	$15 \times D$	$1 \times D$	$105 \times 273 \times 49$	FVM	CDS-2	RK-2	MILES
Parnaudeau et al. [35]	H	$20 \times D$	$20 \times D$	$\pi \times D$	$961 \times 960 \times 48$	HOFDM	CDS-6	AB-2	SF
Mani et al. [27]	O	$70 \times D$	$70 \times D$	$\pi \times D$	$288 \times 396 \times 48$	HOFDM	CDS-6	RK-3	DSM
Meyer et al. [28]	O-H	$30 \times D$	$20 \times D$	$4 \times D$	$6 \times 10^6$	FVM	CDS-2	RK-3	ILES
Meyer et al. [28]	H	$30 \times D$	$20 \times D$	$4 \times D$	$6.5 \times 10^6$	FVM	CDS-2	RK-3	ILES
Ouvrard et al. [34]	UN	$35 \times D$	$40 \times D$	$\pi \times D$	$1.46 \times 10^6$	FEM/FVM	MUSCL	BDF-2	WALE
Wornom et al. [45]	UN	$35 \times D$	$40 \times D$	$\pi \times D$	$1.8 \times 10^6$	FEM/FVM	CDS-2	RK-3	WALE
Current	O	$50 \times D$	$50 \times D$	$\pi \times D$	$300 \times 300 \times 64$	FVM	CDS-2	BDF-2	DKE

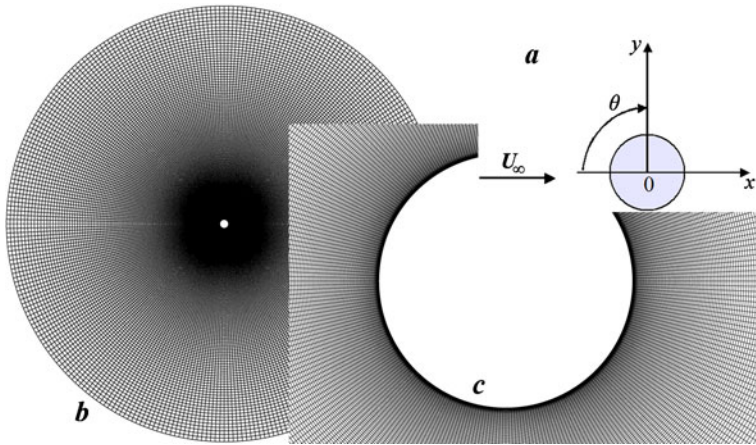


**Fig. 1** General scheme (a), description of the grid (b) and zoom into the cylinder region (c) for the turbulent flow over a circular cylinder at  $Re = 3900$ :  $\theta$  is the circumferential coordinate,  $x$  and  $y$  are the domain extents in stream-wise and transverse directions

the recirculation bubble length). In this context the AR (or the distance between the upper and the lower side of the computational domain) varies significantly from  $L_y = 15 \times D - 70 \times D$ . The largest  $L_y = 70 \times D$  (plus the 'sponge' layer with thickness of  $15 \times D$ ) was used by Mani et al. [27] in their numerical investigation of optical distortions in separated shear layers and turbulent wakes.

Most authors used the same length in the span-wise direction  $L_z = \pi \times D$  discretized by 48 computational nodes. An exception is Kravchenko and Moin [19], who employed  $L_z = 2\pi \times D$ , but with the same grid density. It was found by Kravchenko and Moin [19] and Breuer [3] that doubling the cylinder span from  $\pi \times D$  to  $2\pi \times D$  and keeping the span-wise resolution did not change the results much. Ma et al. [26] performed DNS with a spectral FEM and showed that two converged states of the flow field in the very near wake exist, which are related to shear-layer transition and depend on  $L_z$ . For a domain size of  $2\pi \times D$ , a short recirculation length ( $L_r$ ) is obtained, while  $L_z = \pi \times D$  leads to a long  $L_r$ , if the same span-wise resolution is retained. Recently, Wissink and Rodi [44] performed a series of DNS tests for a flow over a circular cylinder at  $Re = 3300$ . For this purpose Wissink and Rodi employed several O-type grids with a maximum resolution of  $1206 \times 406 \times 1024$ . The span-wise direction was varied from  $4 \times D$  to  $8 \times D$ . It was found that the span-wise size ( $L_z = 4 \times D - 8 \times D$ ) only marginally affected the time-averaged statistics in the cylinder wake. However, the further analysis of the span-wise autocorrelation of the stream-wise velocity indicated that it did not converge to zero for  $L_z \rightarrow 8 \times D$ . These data showed that even a span size of  $8 \times D$  might not be large enough to accommodate all span-wise structures. Wissink and Rodi concluded that to predict the details of the flow around a circular cylinder in the lower sub-critical range correctly, the span-wise length should be even larger than  $8 \times D$  in numerical simulations.

The total mesh size in any LES reference did not exceed  $10 \times 10^6$  nodes. The pioneering simulation conducted by Parnaudeau et al. [35] had a resolution of  $961 \times 960 \times 48$  ( $\approx 45 \times 10^6$ ). Moreover, it is worth noticing that many authors later have

utilized a meshing strategy where the grid is strongly refined near the cylinder in order to describe very accurately the development and detachment of the boundary layer. Parnaudeau et al. [35] adopted the opposite point of view by using a regular grid that leads to a better spatial resolution in the active region of the boundary layer while being significantly less accurate in the near-wall region. Thus, the assumption of the weak influence of the detailed boundary layer structure on the wake statistics was adopted. In spite of this, their LES results showed fairly good agreement with the experimental data. It can be noticed that besides a good resolution of the cylinder boundary layer, it is important to resolve the free shear [44] layers originating from the top and bottom of the cylinder. The further separation of the shear layers leads to arising of the shear-layer instabilities due to the Kelvin–Helmholtz mechanism. An accurate prediction of the characteristic frequencies for this type of instability is important for the high-fidelity LES as well.

In the context of the numerical methods, high-order FDM or FVM were used in most of the cases. For both, the most popular non-dissipative central-differences schemes were applied with different order of approximation (from second order up to sixth order) for the spatial discretization. Runge–Kutta methods (in different realizations) were the most popular for the time integration, however, the fractional step method and the Euler backward method were used by several authors as well. Finally, practically all calculations were done using the eddy-viscosity type SGS model from the simplest one, based on the structure function [35], to the most sophisticated ones, utilizing the dynamic procedure of Germano et al. [12] and Lilly [20]. However, accumulated experience in LES implies that the details of the sub-grid model are of less importance, provided that the grid and the handling of the near-the-wall flow are appropriate [8]. It seems that with a high spatial resolution, it is possible to achieve satisfactory results even with the simplest SGS model formulation [35].

### 1.3 Paper overview

In the present large-eddy simulation, the ‘classical’ O-type grid with a computational domain of  $50 \times D$  was set-up. The spatial grid resolution consisted of  $300 \times 300 \times 64$  grid nodes. The characteristic integration time for sampling data was omitted in Table 1 since it will be discussed in details in Section 4. Here we notice only that in these simulations, the total time of integration was about 150 vortex shedding periods, that is, about two times larger than the largest one used in published LES results. Further, we utilized the unstructured compressible FVM with a global second order accuracy in space and time. We adopted the dynamic  $k$ -equation eddy viscosity SGS model as a ‘baseline’ for this case since it seemed to be the most appreciated choice for reactive (combustion) LES at the moment. In addition, the conventional Smagorinsky model was used to check SGS model sensitivity. It should be noticed that it was not possible to achieve solution without any SGS model at all.

The paper is organized as follows: A general test case description is given in Section 2. In Section 3 the main features of the employed numerical method are summarized. Computational results are presented and analyzed in Section 4, and concluding remarks are given in Section 5.

## 2 Test Case Description

The investigation of the OpenFOAM capabilities for the large-eddy simulation was performed for the flow past a circular cylinder with low (sub-critical) Reynolds ( $Re = 3900$ ) and Mach ( $M = 0.2$ ) numbers.

The curvilinear O-type orthogonal grid (Fig. 1) was used with  $300 \times 300$  control volumes (CV) in the cross-sectional plane and 64 CV in the span-wise direction (total of  $5.76 \times 10^6$  CV). The grid had a span-wise extension  $L_z = \pi \times D$ . The entire computational domain had a radial extension of  $25 \times D$  in the cross-section. The grid points were clustered in the vicinity of the cylinder ( $\Delta r/D = 1 \times 10^{-3}$ ) with a grid expansion factor in the radial direction of 1.085. It can be seen that the grid near the cylinder was only stretched in the radial direction. This was done to avoid the occurrence of numerical inaccuracies due to unfavorable cell aspect ratios [44].

The inlet (left part of the computational domain) boundary conditions were treated as laminar. The reason for not adding perturbations at the inlet was the same as mentioned by Breuer [3]: In the designed grid, the control volumes near the inlet are large because of grid expansion from the surface of the cylinder towards the outlet boundaries. Thus the inflow perturbations will be highly damped, and the probability that these perturbations will reach the cylinder is small. Previous experience showed [3] that in general, this inflow turbulence totally disappears until the flow reaches the cylinder. At the outlet, wave-transmissive conditions [36] were applied. To avoid any kind of wall functions, the boundary layer was resolved by the grid in the near-wall region and isothermal no-slip conditions were applied. In the span-wise direction of the cylinder, periodicity of the flow was assumed. The molecular viscosity and the thermal conductivity were set to be constant. The Prandtl number was assumed to be 0.75, and the ratio of specific heats was 1.4. The compressibility was treated using the ideal gas law. The initial conditions corresponded to the conditions of the sudden stopping of a cylinder in a fluid flow, i.e., the input conditions were extended to the whole computational region.

## 3 Brief Description of Numerics

Large-eddy simulation was carried out using the OpenFOAM code [43] v.1.7.1. The compressible solver rhoPisoFOAM was based on the factorized FVM [13] with the Pressure-Implicit with Splitting of Operators (PISO) algorithm for the pressure-velocity coupling, implemented according to Rhie and Chow type interpolation for the cell-centered data storage structure [16]. The central-difference scheme (CDS-2 [13]) was applied for all convective-term approximations. All inviscid terms and the pressure gradient were approximated with a fourth-order accuracy. A second-order implicit Euler method (BDF-2 [13]) was used for time integration together with the dynamic adjustable time stepping technique to guarantee a local Courant number less than 0.5. A preconditioned (bi-) conjugate gradient method [15] with the incomplete-Cholesky preconditioner (ICCG) by Jacobs [17] was used for solving linear systems with a local accuracy of  $10^{-7}$  for all dependent variables at each time step.

While filtering the compressible flow equations, some sub-grid terms arise, which lead to the need for explicit sub-grid modeling. The Mach number can be used



to characterize the importance of the compressibility effects. For sufficiently low Mach numbers, the effects of compressibility are negligible, and it is sufficient to model the turbulent stress tensor. However, as the Mach number increases, one may expect that explicit sub-grid modeling of the energy equation sub-grid terms becomes necessary. Whether this is the case, and beyond which Mach numbers such modeling is required, depends on the particular flow and the accuracy with which the flow needs to be represented. Compared to incompressible LES, much less research has been conducted on compressible LES [11]. However, in *a-posteriori* tests reported in [41] it was found that explicit sub-grid modeling for the energy equation was not needed for Mach numbers up to 0.6. The effects were more pronounced at  $M = 1.2$ , and the use of the dynamic eddy-viscosity model showed an accurate capturing of the decay of the kinetic energy. The main argument was that most of the compressibility effects are assumed to affect essentially the large scales. In the present study the compressible flow was calculated at the particular Mach number,  $M = 0.2$ . Thus additional terms arising from the filtration of the energy equation were not taken into account, assuming sub-grid scales incompressibility hypothesis [11].

The dynamic  $k$ -equation eddy-viscosity SGS model (TKE hereafter) and the conventional Smagorinsky SGS model [39] (SMAG hereafter) were chosen to close the equations. One can find some theoretical background for both models in the studies provided by Fureby [9] and Fureby et al. [10]. It should be noticed that Fureby denoted SMAG and TKE models as constant coefficient algebraic eddy-viscosity and dynamic coefficient one-equation eddy-viscosity, respectively.

Both models are based on the SGS kinetic energy  $k = \frac{1}{2} (\tilde{\mathbf{v}}^2 - \tilde{\mathbf{v}}^2)$ , where  $\tilde{\mathbf{v}}$  is the filtered density weighted velocity. The following assumptions for the SGS density weighted stress tensor  $\mathbf{B}$  and the filtered deviatoric part of the rate of strain tensor  $\tilde{\mathbf{D}}_D$  are used:

$$\mathbf{B} = \frac{2}{3} \bar{\rho} k \mathbf{I} - 2\mu_B \tilde{\mathbf{D}}_D, \quad (1)$$

$$\tilde{\mathbf{D}}_D = \left[ \tilde{\mathbf{D}} - \frac{1}{3} (\text{tr } \tilde{\mathbf{D}}) \mathbf{I} \right], \quad (2)$$

$$\tilde{\mathbf{D}} = \frac{1}{2} (\text{grad } \tilde{\mathbf{v}} + \text{grad } \tilde{\mathbf{v}}^T), \quad (3)$$

$$\mu_B = c_k \bar{\rho} \sqrt{k} \Delta, \quad (4)$$

where  $\mathbf{I}$  is the unit tensor,  $\bar{\rho}$  is the filtered density,  $\mu_B$  is the SGS viscosity and  $\Delta$  represents the top-hat filter with a characteristic filter width estimated as the cubic root of the CV volume (that applied as filter kernel). An exact balance equation for  $k$  can be derived, but some terms must be modeled. Instead, following Fureby [9] this balance equation can be replaced by the *a posteriori* modeled equation:

$$\partial_t(\bar{\rho} k) + \text{div}(\bar{\rho} \tilde{\mathbf{v}} k) = \mathbf{F}_p + \mathbf{F}_d - \mathbf{F}_\varepsilon, \quad (5)$$

$$\mathbf{F}_p = -\mathbf{B} \cdot \tilde{\mathbf{D}}, \quad \mathbf{F}_d = \text{div}((\mu_B + \mu) \text{grad } k), \quad \mathbf{F}_\varepsilon = c_\varepsilon \bar{\rho} k^{3/2} / \Delta,$$

where  $\mathbf{F}_p$  is production,  $\mathbf{F}_d$  diffusion and  $\mathbf{F}_\varepsilon$  dissipation terms, respectively.



The conventional Smagorinsky SGS model can be recovered from Eq. 5 by assuming local equilibrium, i.e.,  $\mathbf{F}_p = \mathbf{F}_\varepsilon$ . Thus, the SGS kinetic energy can be computed from the following relation:

$$\mathbf{B} \cdot \tilde{\mathbf{D}} + c_\varepsilon \bar{\rho} k^{3/2} / \Delta = 0. \quad (6)$$

Using Eq. 1 and introducing the coefficients

$$a = \frac{c_\varepsilon}{\Delta}, \quad b = \frac{2}{3} \text{tr } \tilde{\mathbf{D}}, \quad c = -2c_k \Delta \tilde{\mathbf{D}}_D : \tilde{\mathbf{D}}, \quad (7)$$

the relation in Eq. 6 can be reformulated by the quadratic equation to the relation for  $k$

$$k = \left( \frac{-b + \sqrt{b^2 - 4ac}}{2a} \right)^2. \quad (8)$$

The models constants are:  $c_k = 0.02$  and  $c_\varepsilon = 1.048$ . The relationship between the classical  $C_s$  constant and the default constants  $C_k$  and  $C_\varepsilon$  from the Smagorinsky model implementation in OpenFOAM is  $C_s = (c_k^3 / c_\varepsilon)^{1/4}$ , which leads to a value  $C_s = 0.053$ . This value is slightly lower than the minimum conventional limit  $C_s = 0.065$ . It is worth noting that this relation can be recovered from the classical assumption (gradient hypothesis) for the eddy-viscosity  $\mu_B = (C_s \Delta)^2 \bar{\rho} \|\tilde{\mathbf{D}}\|$  and Eq. 4.

The dynamic model for the  $k$  equation can be derived using the Germano identity  $\mathbf{L}$  with another filter kernel of width  $\bar{\Delta} = 2\Delta$ . Again, one can find the theoretical background in the studies performed by Fureby [9] and Fureby et al. [10]. Here, we will concentrate on the model implementation only.

The model coefficient  $c_k$  can not be removed from filtering and hence, a variational formulation is used to evaluate this:

$$c_k = \frac{\langle \mathbf{L}_D \cdot \mathbf{M} \rangle}{\langle \mathbf{M} \cdot \mathbf{M} \rangle}, \quad (9)$$

where  $\mathbf{M} = \Delta(\overline{k^{1/2} \tilde{\mathbf{D}}} - 2(K + \bar{k})^{1/2} \tilde{\mathbf{D}})$ ,  $\mathbf{L}_D = (\tilde{\mathbf{v}}^2 - \bar{\mathbf{v}}^2)_D$  and  $K = \frac{1}{2}(\|\tilde{\mathbf{v}}\|^2 - \|\bar{\mathbf{v}}\|^2)$ .

The second coefficient  $c_\varepsilon$  is defined as

$$c_\varepsilon = \frac{\langle \zeta \cdot \mathbf{M} \mathbf{M} \rangle}{\langle \mathbf{M} \mathbf{M} \cdot \mathbf{M} \mathbf{M} \rangle}, \quad (10)$$

where  $\zeta = 2\Delta c_k (\overline{k^{1/2} \|\tilde{\mathbf{D}}\|^2} - 2(K + \bar{k})^{1/2} \|\tilde{\mathbf{D}}\|^2)$  and  $\mathbf{M} \mathbf{M} = (K + \bar{k})^{3/2} / 2\Delta - \bar{k}^{3/2} / \Delta$ .

OpenFOAM is the massive parallel open source C++ classes library based on message-passing interface (MPI). Since the assessment of the parallel performance is useful, OpenFOAM, both in terms of strong and weak scalability, was tested at the Stallo high-performance computing (HPC) facility (HP BL 460c cluster) (<http://www.notur.no>) within up to 1024 processors. OpenFOAM showed a modest parallel performance with an efficiency of  $\approx 50\%$  [24]. The present calculations were carried out at Stallo using 256 cores in parallel. The calculation time for one time step was around 3 s, and the total simulation time for one run was  $\approx 226$  h. With respect to parallel performance, application of the conventional Smagorinsky model was  $\approx 20\%$  more efficient compared to the use of the dynamic  $k$ -equation model.

## 4 Results

In the literature, numerical or experimental studies on the convergence of the principal turbulence statistics are scarce. Franke and Frank [7] studied this point and concluded that more than 40 shedding periods are required to obtain converged mean flow statistics. The results performed by Parnaudeau et al. [35], Mani et al. [27] and Meyer et al. [28] were based on the collected data of about 60 vortex shedding cycles. For a quantitative validation in the present simulation, turbulence statistics were sampled over 150 shedding cycles (time interval of  $TU_\infty/D = 700$ ) after quasi-steady vortex shedding was established. The turbulent wake has been considered as fully established after a duration of  $TU_\infty/D = 700$ . Statistics were averaged in the periodic span-wise direction as well. The averaging operator is denoted by  $\langle \rangle$ .

The results were compared with pressure measurements of Norberg [31], the PIV data of Lourenco and Shih [21], the HWA of Ong and Wallace [33] and the PIV data of Parnaudeau et al. [35] and DNS of Wissink and Rodi, Case E [44]. DNS results of Dong et al. [6] were used to analyze shear-layer instability.

### 4.1 Instantaneous flow field

Figure 2 demonstrates the time histories of the present lift ( $C_l$ ) and drag ( $C_d$ ) coefficients for a period of  $\approx 150$  vortex shedding cycles for both LES runs (SMAG and TKE, respectively). The drag coefficient per unit length is  $C_d = 2F_x/\rho_\infty U_\infty^2 D$ , where  $F_x$  is the force acting in the stream-wise direction at the boundary of the

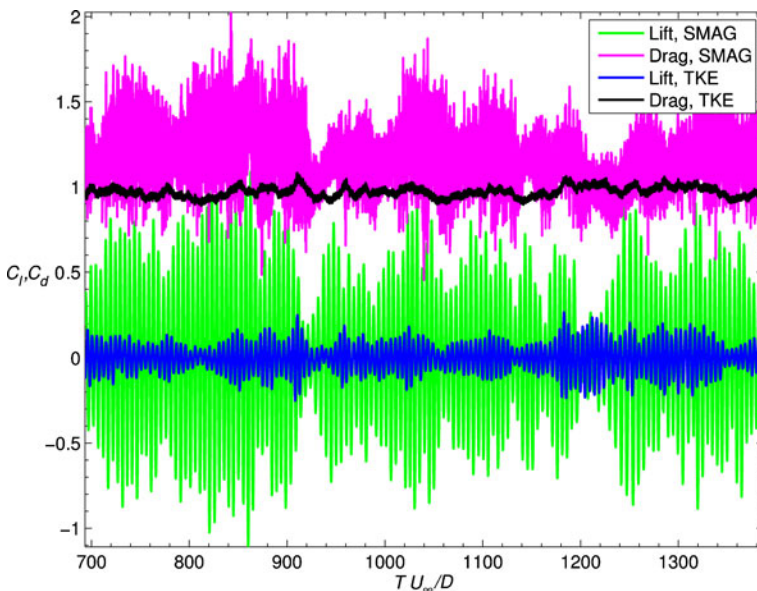


**Fig. 2** Time history of the lift  $C_l$  and drag  $C_d$  coefficients ( $\approx 150$  vortex shedding cycles) for the conventional Smagorinsky (SMAG) and the dynamic  $k$ -equation (TKE) SGS models for the flow over a circular cylinder at  $Re = 3900$

obstacle. The lift coefficient per unit length is, like the drag coefficient, defined as  $C_l = 2F_y/\rho_\infty U_\infty^2 D$ , where  $F_y$  is the force acting in the transverse direction at the boundary of the obstacle. The total force  $F$  consists of the friction force  $F_f$  and the pressure force  $F_p$ . The irregularity in the forces may be explained by the irregular three-dimensional break up of the vortices. It is interesting that the magnitudes of the lift and drag coefficients obtained by the dynamic  $k$ -equation model were significantly lower than those predicted by the conventional Smagorinsky model. This finding may be explained by the formation of the free shear layers from the cylinder surface. As the boundary layer from the upper and lower parts of the cylinder surface detaches, free-shear layers are formed. This process is displayed in Fig. 3. One can see that the transition from 2D to 3D flow takes place very close at the cylinder surface for the solution obtained by SMAG model, which immediately affects the drag and lift forces. At the same time, the TKE solution was characterized by long, mainly two-dimensional, free-shear layers with a stream-wise length of approximately  $2 \times D$ . The location of a span-wise modulation corresponded to the onset of the laminar-turbulent transition. The forces in the TKE case were more smoothed, which corresponds to features of a laminar flow.

The root-mean-square values of the time variation of the drag and lift coefficients predicted by the SMAG and TKE models were  $(C_l)_{\text{rms,SMAG}} = 0.444$ ,  $(C_d)_{\text{rms,SMAG}} - \langle C_{d,\text{SMAG}} \rangle = 0.01$  and  $(C_l)_{\text{rms,TKE}} = 0.089$ ,  $(C_d)_{\text{rms,TKE}} - \langle C_{d,\text{TKE}} \rangle = 0.0005$ , respectively. To assess these values more precisely, we compared them with numerical [34, 45] and experimental [32] data available in the literature. From the experimental point of view, a comprehensive analysis has been done by Norberg [32], where the numerous measured data for the fluctuating lift coefficient were gathered. However, according to Norberg [32], a significant scatter of the measured data is observed, and in particular for  $\text{Re} = 3000 - 5000$  the fluctuating lift coefficient varies from  $(C_l)_{\text{rms}} = 0.03 - 0.1$ . Several LES studies with some information related to the fluctuating lift and drag forces are available in the literature as well. Ouvrard et al. [34] examined the effect of the SGS model and revealed the strong correlation between the amount of introduced SGS viscosity and the flow evolution downstream the cylinder which leads to a strong variation of the oscillating loads. They observed  $(C_l)_{\text{rms}} = 0.051 - 0.604$  and  $(C_d)_{\text{rms}} = 0.014 - 0.072$  depending on the

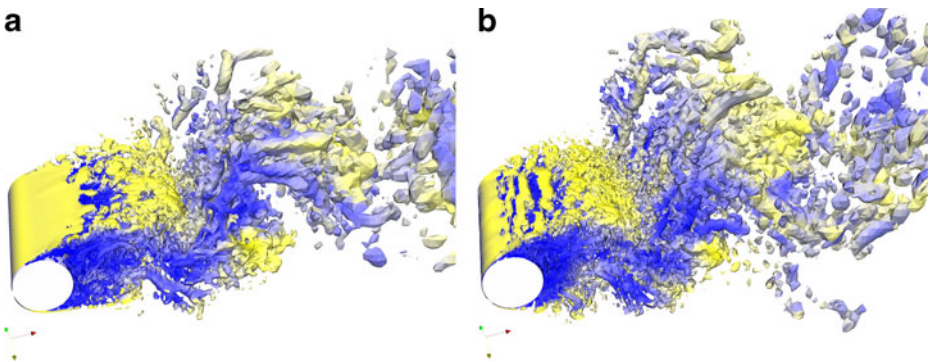


**Fig. 3** Iso-surface of normalized  $\lambda_2 = 0.004$  obtained by TKE (a) and SMAG (b) for the flow over a circular cylinder at  $\text{Re} = 3900$ .  $\lambda_2$  was defined according to Jeong and Hussain [18]

SGS model and the grid resolution. Some observations from the study by Ouvrard et al. [34] were: (1) the larger the SGS viscosity introduced by the model, the more upstream the shear-layer transition occurs, and the vortices form; (2) a shorter mean recirculation bubble length corresponds to a higher amplitude of  $(C_l)_{\text{rms}}$  and  $(C_d)_{\text{rms}}$ . The present calculations confirmed these statements. The results obtained by TKE seem to be in good agreement with the experimental data and with the recent results presented by Wornom et al. [45] carried out with variational multiscale large-eddy simulations ( $(C_l)_{\text{rms}} = 0.108$ ). As mentioned above, no adaptation of the Smagorinsky model constants were carried out and the default values of  $c_k$  and  $c_\varepsilon$  were used. It has been known that the lower value of  $C_s$  leads to the lower level of the SGS viscosity. Indeed, the recirculation zone length obtained by SMAG was approximately 1.85 times shorter compared to TKE (see Section 4.2), and the SMAG model had the less dissipative energy spectrum (Section 4.4), giving the highest values of  $(C_l)_{\text{rms}}$  and  $(C_d)_{\text{rms}}$  (Fig. 2).

Figure 4 illustrates the formation of the vortex street somewhat downstream of the circular cylinder, showing an iso-surface of the fluctuating pressure  $p' = 2(p - \langle p \rangle) / \rho_\infty U_\infty^2$ . The iso-surface identifies the vortex cores that originate from the roll-up of the shear layers from the upper and lower parts of the cylinder surfaces. These vortices are parallel to the cylinder axis and are convected further downstream by the mean flow.

#### 4.2 Mean flow features

The distribution of the mean pressure coefficient ( $\langle C_p \rangle = 2(\langle p \rangle - p_\infty) / \rho_\infty U_\infty^2$ , where  $p_\infty$  and  $\rho_\infty$  are the free stream pressure and density, respectively) on the cylinder's surface is plotted in Fig. 5a. The calculated data by TKE were in good agreement with the measured values provided by Norberg [31]. However, there are some deviations between the experimental and SMAG data. The detailed analysis of the flow field in the near wake calculated by SMAG revealed the existence of a



**Fig. 4** Iso-surface of the fluctuating pressure at  $p' = -0.1$  (TKE) for the flow over a circular cylinder at  $Re = 3900$

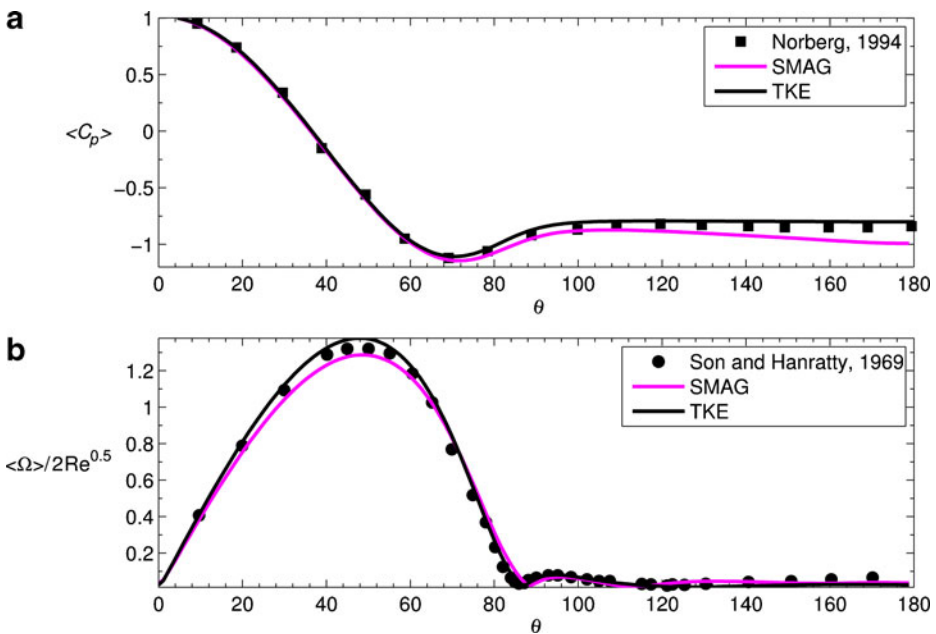
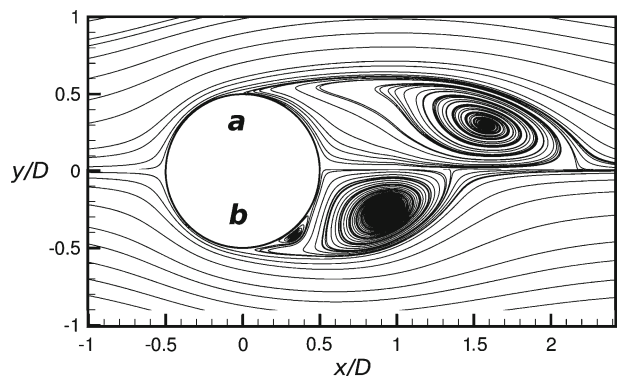


**Fig. 5** Mean pressure coefficient (a) and mean, normalized vorticity magnitude (b) distributions on the cylinder surface ( $\theta_{sep} = 0$  is the stagnation point) for the flow over a circular cylinder at  $Re = 3900$

small counter-rotating vortex (beside the main recirculation bubble) attached to the backward side of the cylinder (Fig. 6b). This finding means that several separation angles (beside the primary  $\theta_{sep}$ ) existed in the SMAG solution. Breuer [3] got the same results in a LES study, using the HYBRID (a combination of the upwind and the central-difference approximations) and HLP (hybrid linear/parabolic approximation) schemes. From the experimental point of view, the existence of the small vortices at the backward side of the cylinder was confirmed by Son and Hanratty [40]. In Fig. 5b the mean vorticity magnitude (which was non-dimensionalized with the

**Fig. 6** Time-averaged streamlines in the  $x$ - $y$  plane by TKE (a) and SMAG (b) runs for the flow over a circular cylinder at  $Re = 3900$



factor  $2\sqrt{\text{Re}}$ , according to Ma et al. [26]) is plotted along with experimental data. The agreement between the numerical and experimental results was fairly good starting from the stagnation point  $\theta_{\text{sep}} = 0^\circ$  till  $\theta \approx 120^\circ$ . The mean, prime separation angle  $\langle\theta_{\text{sep}}\rangle$  is determined from the condition of vanishing wall-shear stress. As known from measurements [21], the separation should take place at  $\langle\theta_{\text{sep}}\rangle = 86^\circ$ . The calculated values of  $\langle\theta_{\text{sep}}\rangle$  from the most cited LES runs are in the range of  $\langle\theta_{\text{sep}}\rangle = 87 - 88^\circ$ . The predicted  $\langle\theta_{\text{sep}}\rangle = 88^\circ$  by TKE and  $\langle\theta_{\text{sep}}\rangle = 89^\circ$  by SMAG were slightly higher than the experimental results and were consistent with previous LES data [3, 7, 19, 28, 30, 45]. At the backward side of the cylinder, the TKE solution was quite similar to the experimental data of Son and Hanratty [40]. However, it did not represent secondary vorticity structures besides the main recirculation zone. The length of the secondary separation zone predicted by SMAG was  $\theta \approx 25^\circ$ , while the measured value by Son and Hanratty [40] was  $\theta \approx 35^\circ$ .

The mean base suction coefficient  $\langle C_{p,b} \rangle$  can be determined as the mean pressure coefficient on the cylinder's surface at  $\theta = 180^\circ$ . The calculated value of the mean base suction coefficient by TKE was  $\langle C_{p,b} \rangle = -0.91$ , which correlates well with the experimental value obtained by Norberg [31], who measured  $\langle C_{p,b} \rangle = -0.90$ . At the same time, the predicted value of  $\langle C_{p,b} \rangle$  by SMAG was approximately 10 % lower ( $\langle C_{p,b} \rangle = -0.8$ ), which was close to the results by Franke and Frank [7] ( $\langle C_{p,b} \rangle = -0.85$ ) and Mani et al. [27] ( $\langle C_{p,b} \rangle = -0.86$ ).

The base suction coefficient is strongly related to the drag coefficient. The calculated mean drag coefficient  $\langle C_d \rangle = 0.97$  by TKE was in good agreement with the experimental data of Lourenco and Shih [21] and Norberg [31]. However, it is worth noticing that most values of the drag coefficient obtained in the literature with different LES techniques are slightly higher ( $\langle C_d \rangle = 0.99 - 1.07$ ). Most of these LES-based results were obtained with an incompressible flow assumption. Several published LES results for  $\langle C_d \rangle$ , obtained with compressible solvers [7, 27, 45], are within the range of  $\langle C_d \rangle = 0.97 - 0.99$  and correlate well with experimental data and the present calculations. The drag coefficient predicted by SMAG was higher ( $\langle C_d \rangle = 1.17$ ) and close to the results by Breuer [3] and Meyer et al. [28] ( $\langle C_d \rangle = 1.07 - 1.1$ ).

The difference between measurements and numerical calculations for the mean recirculation zone length  $\langle L_r \rangle$  is significant and often subject to discussion. By definition, the recirculation length  $\langle L_r \rangle$  corresponds to the distance between the base of the cylinder and the sign change of the centerline mean stream-wise velocity. The quality of  $\langle L_r \rangle$  predictions may be considered as the deciding factor about the agreement between the experimental and numerical results [35]. According to Kravchenko and Moin [19], the observed variation can be affected by the earlier laminar-turbulence transition in the separating shear layers of the experiment. A lack of statistical convergence can also be suggested [35]. Norberg [31] showed that aspect ratios of 60–70 are required for obtaining unaffected results in lab test conditions. Moreover, the experiments of Ong and Wallace [33] and Parnaudeau et al. [35] were carried out with the same aspect ratio ( $AR \approx 21$ ) but disagree significantly with each other. The minimum values of the  $\langle L_r \rangle$  were measured by Lourenco and Shih [21] ( $\langle L_r \rangle / D = 1.19$ ). Recent PIV data, provided by Dong et al. [6] and Parnaudeau et al. [35], revealed a more extended recirculation zone length  $\langle L_r \rangle / D = 1.36 - 1.51$ . In the context of the numerical simulations that were performed supporting these experiments (DNS by Dong et al. [6] and Ma et al. [26] and LES by Parnaudeau et al. [35]), the length of the recirculation bubble was reported in the range  $\langle L_r \rangle / D =$



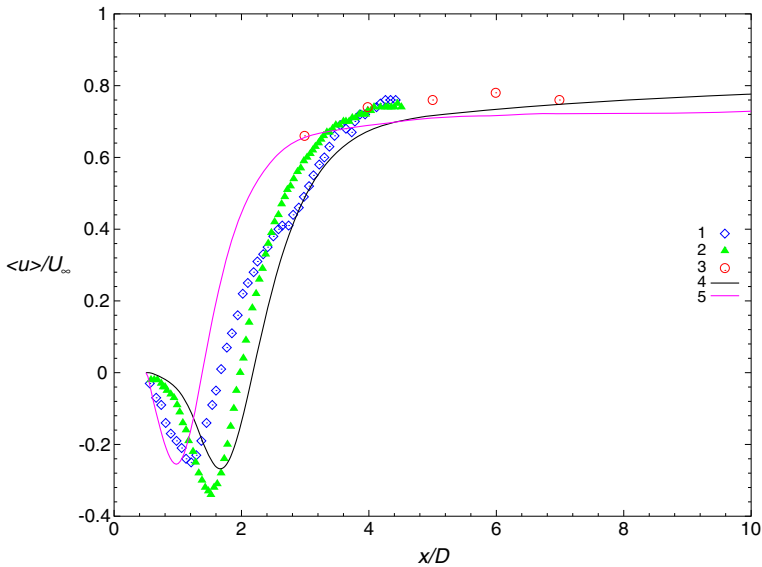


**Fig. 7** Mean stream-wise velocity in the wake centerline for the flow over a circular cylinder at  $Re = 3900$  (1 experiment by of Lourenco and Shih [21], 2 experiment by Parnaudeau et al. [35], 3 experiment by Ong and Wallace [33], 4 present LES-TKE, 5 present LES-SMAG)

1.41 – 1.59 and  $\langle L_r \rangle / D = 1.56$ , respectively. DNS performed by Wissink and Rodi [44] determined the recirculation zone length to  $\langle L_r \rangle / D = 1.588$ .<sup>1</sup>

Further, Parnaudeau et al. [35] reported their experience on the sensitivity analysis of  $\langle L_r \rangle$  with respect to the averaging time interval. They performed a low-resolution LES study with collecting statistics at  $N_{vp} \approx 420$  (where  $N_{vp}$  is the number of vortex shedding periods). Based on this cumulative average statistics, Parnaudeau et al. [35] proposed a converged value  $\langle L_r \rangle / D \approx 1.67$ . Moreover, a recirculation bubble of  $\langle L_r \rangle / D = 1.64$  was reported by Franke and Frank [7], who computed the flow over a circular cylinder at  $Re = 3900$  using an LES solver for compressible flows ( $M = 0.2$ ). It is interesting that Franke and Frank [7] discussed their observations of mean flow quantities ( $\langle C_d \rangle$ ,  $\langle C_{p,b} \rangle$ ,  $\langle \theta_{sep} \rangle$  and  $\langle L_r \rangle$ ) dependency from the averaging interval. Franke and Frank [7] reported the results for the maximum averaging time of  $N_{vp} = 42$  and concluded that it was not sufficient to reach a statistically converged mean flow field. When changing the statistics interval from  $N_{vp} = 10$  to  $N_{vp} = 42$ , mean flow features such as  $\langle C_d \rangle$ ,  $\langle C_{p,b} \rangle$  and  $\langle \theta_{sep} \rangle$  were getting smaller, however the length of the recirculation zone was getting larger.

In the present LES on the one hand, the recirculation zone length was predicted by TKE as  $\langle L_r \rangle / D = 1.67$ , which was in a fairly good agreement with data of Parnaudeau et al. [35]. On the other hand, the recirculation zone length predicted by SMAG was  $\langle L_r \rangle / D = 0.9$ , which was close to data of Lourenco and Shih [21]. Figures 5 and 6 summarize these findings based on the time-averaged streamlines

<sup>1</sup>From private communications.



plots. It is worth noticing that in the present simulations statistics were collected for  $N_{vp} \approx 150$ . Additionally, the present observations showed that the converged value of  $\langle L_r \rangle$  was reached after sampling of the statistics for  $N_{vp} \approx 75$ .

#### 4.3 First-order statistics

The mean stream-wise velocity  $\langle u \rangle$  along the centerline is shown in Fig. 7. One can clearly see that the experiments of Lourenco and Shih [21] and Parnaudeau et al. [35] were quite different from each other. The present predictions of  $\langle u \rangle$  by TKE were close to the PIV experiment of Parnaudeau et al. [35] and the HWA measurements of Ong and Wallace [33]. However, the present results by SMAG were close to the PIV of Lourenco and Shih [21].

There was a slight shift of the calculated  $\langle u \rangle$  from these experiments because of the overestimated (TKE) and underestimated (SMAG) recirculation bubble lengths. The minimum value of the mean stream-wise velocity predicted in the current simulation  $\langle u_{\min} \rangle / U_\infty = -0.27 - -0.26$  was consistent with the values measured by Lourenco and Shih [21] and by Dong et al. [6]. The LES results published by Breuer [3], Parnaudeau et al. [35] and Meyer et al. [28] were also in the range  $\langle u_{\min} \rangle / U_\infty = -0.26 - -0.23$ .

Figures 8, 9, 10, and 11 compare the statistics for the near wake ( $1 \leq x/D \leq 10$ ) of the cylinder with the experiments of Lourenco and Shih [21] and Parnaudeau et al. [35] at three different downstream locations in the very near wake ( $x/D = 1.06, 1.54, 2.02$ ) and with the experiments of Ong and Wallace [33] at three downstream locations in the near wake ( $x/D = 4.00, 7.00, 10.00$ ).

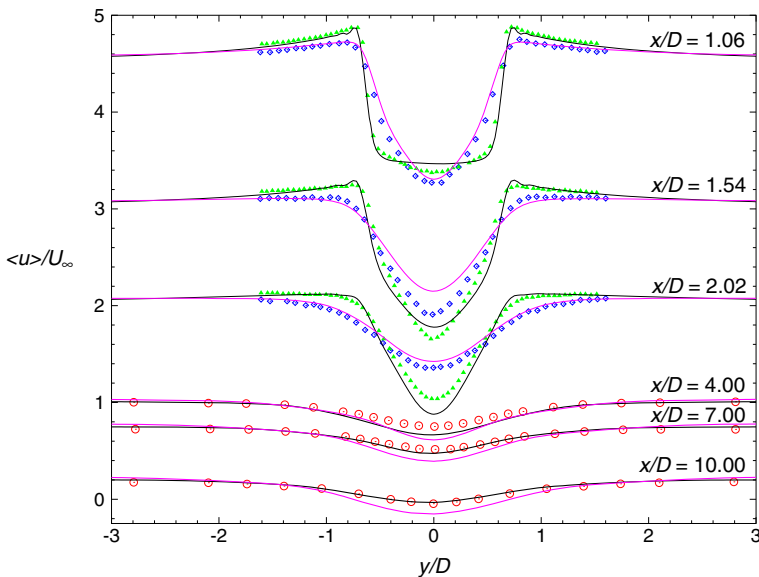


**Fig. 8** Mean stream-wise velocity at different locations in the wake of a circular cylinder at  $Re = 3900$ . For details, see the caption for Fig. 7

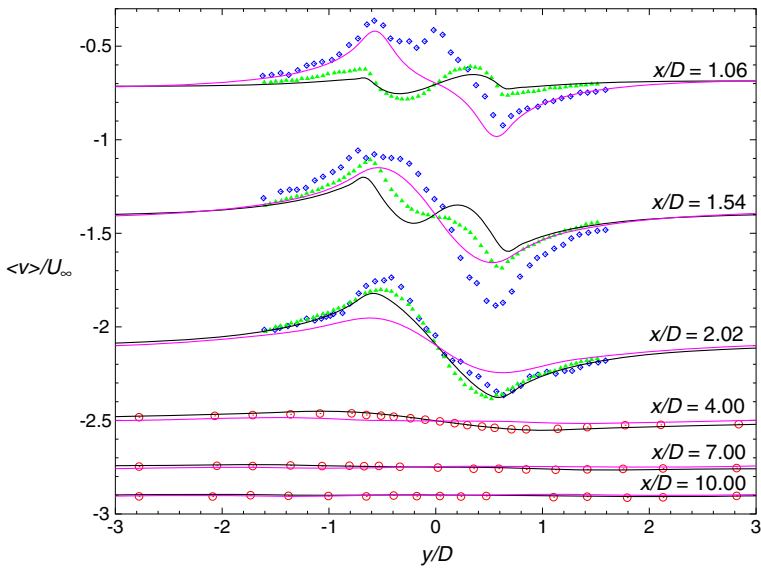


**Fig. 9** Mean transverse velocity at different locations in the wake of a circular cylinder at  $Re = 3900$ . For details, see the caption for Fig. 7

Figure 8 shows velocity profiles for the mean stream-wise velocity  $\langle u \rangle / U_\infty$ . A strong velocity deficit occurred in the region of the recirculation bubble. One can observe the different shapes of the profiles at  $x/D = 1.06$  for the two experimental

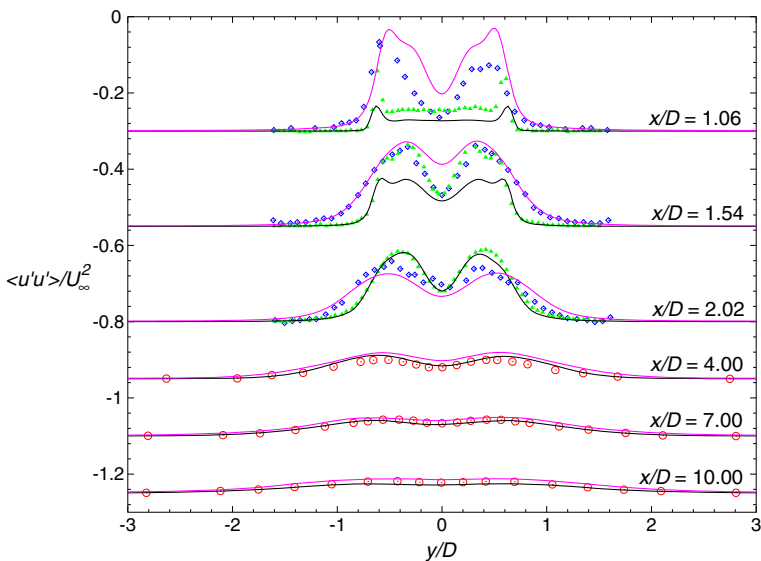


**Fig. 10** Stream-wise velocity fluctuations at different locations in the wake of a circular cylinder at  $Re = 3900$ . For details, see the caption for Fig. 7

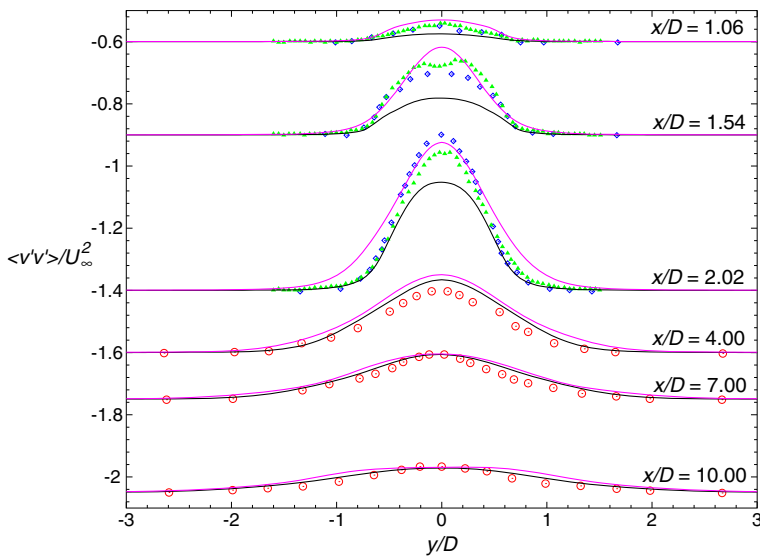


**Fig. 11** Transverse velocity fluctuations at different locations in the wake of a circular cylinder at  $Re = 3900$ . For details, see the caption for Fig. 7

sets as well as for the two present LES runs. The mean velocity profiles obtained by TKE showed a U-shape close to the cylinder, which evolves towards a V-shape further downstream. At the same time, the velocity profiles calculated by SMAG showed a V-shape profile. In the very near wake ( $1 < x/D < 4$ ), the present TKE calculations agreed fairly well with the experimental and LES results of Parnaudeau et al. [35]. The present SMAG calculations agreed fairly well with the experiment of Lourenco and Shih [21]. The calculated  $\langle u \rangle / U_\infty$  profiles at the near wake obtained by SMAG and TKE were in a good agreement with the hot-wire measurements of Ong and Wallace [33].

Results for the mean transversal velocity  $\langle v \rangle / U_\infty$  are shown in Fig. 9. It should be mentioned that the profiles of Lourenco and Shih [21] were shifted so that  $\langle v \rangle = 0$  is recovered for large  $y/D$ , as also done by Franke and Frank [7] and Meyer et al. [28]. As noticed by Meyer et al. [28] and Parnaudeau et al. [35], this anomalous behavior in the data of Lourenco and Shih [21] can be attributed to experimental disturbances. Again, the present TKE and SMAG results were in fairly good agreement with the experiments of Parnaudeau et al. [35] and Lourenco and Shih [21], respectively, in this region. In the near wake, both TKE and SMAG results agreed well with the data of Ong and Wallace [33].

In Fig. 10 the Reynolds normal stresses  $\langle u'u' \rangle / U_\infty^2$  are shown. At  $x/D = 1.06$ , the  $\langle u'u' \rangle$ -profile presents two strong peaks mainly due to the transitional state of the shear layers, which show a flapping behavior due to primary vortex formation [35]. The position of these two peaks agreed with the experiment of Parnaudeau et al. [35], but the magnitudes of the peaks were underestimated for the TKE results. At the same time, the present SMAG data satisfactory agreed with the experimental data of Lourenco and Shih [21] at  $x/D = 1.06$  and  $x/D = 1.54$ . At  $x/D > 1.06$ , the two peaks of the shear layers were overlapped by two larger peaks due to primary vortex

formation. The Reynolds normal stresses were somewhat underestimated in the TKE results compared to the measured data at  $x/D = 1.54$ . This is again probably due to the over-prediction of the recirculation zone length. A good agreement was observed between the present TKE and SMAG results and the experimental data of Parnaudeau et al. [35] and Lourenco and Shih [21] at  $x/D = 2.02$  and, further downstream the wake, with the HWA-data of Ong and Wallace [33].

A satisfactory agreement was found for the cross-flow normal Reynolds stresses  $\langle v'v' \rangle / U_\infty^2$  between the experiments of Lourenco and Shih [21] and Parnaudeau et al. [35] in the very near wake. The present SMAG results showed a quite good agreement in the very near wake as well as in the near wake. However, the present TKE results showed only reasonable agreement of the cross-flow normal Reynolds stresses  $\langle v'v' \rangle / U_\infty^2$  in the very near wake and fairly good agreement in the near wake. This underestimation of the Reynolds stresses implies that the laminar-turbulent transition of the separated shear layers occurs further to the cylinder, which leads to a longer length of the recirculation zone [28].

In general, the present results by TKE and SMAG agreed fairly well with the experimental data. For the very near wake, the LES based on the dynamic  $k$ -equation SGS model was close to the experimental data set of Parnaudeau et al. [35], and the LES results based on the conventional Smagorinsky model matched the data of Lourenco and Shih [21]. For the near wake, both the present LES results were in good agreement with the HWA-data of Ong and Wallace [33]. Some deviations are observed between the present TKE results and the experimental data for the Reynolds normal and cross-flow normal stresses in the very near wake ( $x/D = 1.06$  and  $x/D = 1.54$ ). Figure 12 compares profiles of  $\langle u'u' \rangle / U_\infty^2$  from numerical data by Wissink and Rodi [44] and Ma et al. [26] and the present TKE results. The LES

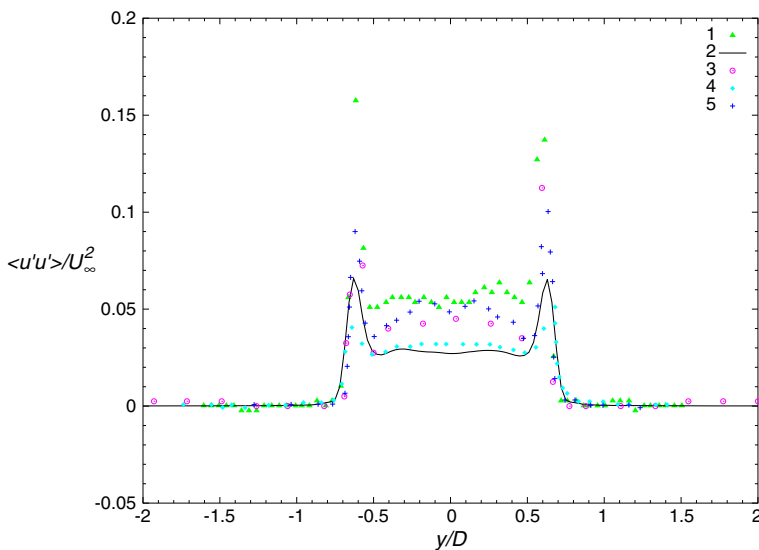


**Fig. 12** Stream-wise velocity fluctuations at  $x/D = 1.06$  in the wake of a circular cylinder at  $Re = 3900$  1 experiment by Parnaudeau et al. [35], 2 present LES-TKE, 3 DNS by Wissink and Rodi [44], 4 LES by Ma et al. [26], 5 DNS by Ma et al. [26]

results by Ma et al. were in good agreement with the present calculations. The DNS data by Wissink and Rodi [44] and Ma et al. shown somewhat higher predicted Reynolds stresses than in the present LES data. However, even the DNS data [26, 44] did not reproduce the peak values of the experiment by Parnaudeau et al. [35] correctly.

#### 4.4 One-dimensional energy spectra

The flow over a circular cylinder at  $Re = 3900$  is referred to as a flow in the ‘sub-critical regime’ where the circular-cylinder boundary layer stays laminar until  $1000 < Re < 200000$ . The dynamics of the downstream flow field behind a cylinder is largely driven by the shear layer and wake processes alone. For this  $Re$  range, both absolute and convective instabilities are present—symmetric vortex shedding (the Bénard/von Kármán instability) and Kelvin-Helmholtz (KH) instability of the separated shear layer [37]. The vortex shedding instability is periodic and has a characteristic frequency of  $f_{vs} = StU_\infty/D$ , where  $St$  is the Strouhal number in the post-shear-layer transition. The Strouhal number determined from a Fast Fourier transform of the  $C_l$  time signal and obtained by TKE (Fig. 2) was  $St = 0.209$ . This value was in good agreement with the experimental predictions by Ong and Wallace [33] ( $St = 0.21$ ) and Parnaudeau et al. [35] ( $St = 0.208$ ). The Strouhal number predicted by SMAG was slightly lower  $St = 0.19$  and corresponds to the DNS data by Dong et al. [6], who reported  $St = 0.2$ .

Figure 13 compares one-dimensional frequency spectra extracted from the present solutions by SMAG and TKE at the downstream location ( $x/D = 3$  and  $x/D = 5$ ) on the centerline of the wake. About  $10^5$  samples of the cross-flow velocities were collected over a dimensionless time interval  $TU_\infty/D \approx 350$  (or  $N_{vp} \approx 73$ ). The spectra calculated from these time series were then averaged in the span-wise direction to increase the statistical sample [19]. Since an adaptive-time stepping technique was used for the time integration (due to varying time steps), the collected time series were not evenly sampled. To obtain the spectra, the Welch periodogram technique [42] was used for the two signal sequences of 36 vortex shedding cycles with overlapping factor of 0.7. The frequency was nondimensionalized by Strouhal shedding frequency ( $f_{vs}$ ). The power spectra are displayed together with the experimental results of Ong and Wallace [33] and Parnaudeau et al. [35]. A  $-5/3$  slope is shown as well. Both of the measured data sets yielded very similar power spectra. The overall agreement between experimental and numerically predicted spectra is good at both locations. Ma et al. [26] and Kravchenko and Moin [19] noticed that the effect of an excessive dissipation of a numerical method led to a rapid decay of the spectrum so that no inertial subrange could be satisfactorily captured. Contrary to this, the spectrum obtained by LES based on non-dissipative schemes matched the experimental data better. In the current simulations the inertial subrange was reproduced clearly for a large spectral range, assuming that sub-grid modeling was not over-dissipative. Moreover, as was reported by Kravchenko and Moin [19] and Parnaudeau et al. [35], the spectra were also consistent with the presence of small scales that remain active far from the cylinder (Fig. 3). However, it is worth noting that the spectra obtained by SMAG seem to be less dissipative compared to that obtained by TKE. One can observe this finding in Fig. 13b, where the TKE spectrum starts to decay rapidly just before the grid frequency cut-off.

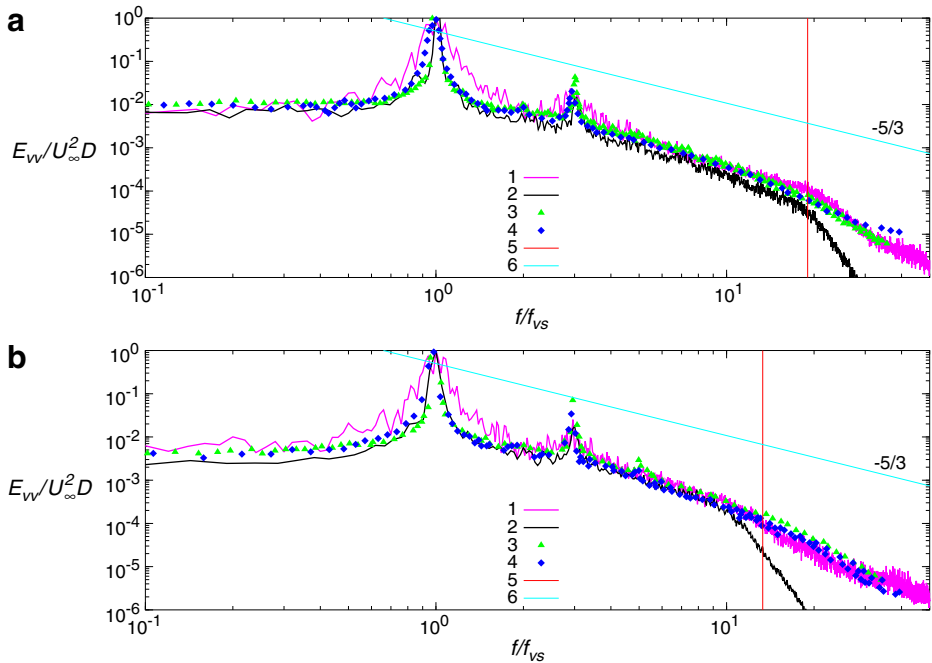


**Fig. 13** One-dimensional spectra of the transverse velocity in the wake of a circular cylinder at  $Re = 3900$  at  $x/D = 3$  (**a**) and  $x/D = 5$  (**b**): 1—present LES-SMAG; 2—present LES-TKE; 3—experiment by Parnaudeau et al. [35] with cut-off frequency  $f/f_{vs} < 35$ ; 4—experiment by Ong and Wallace [33] with cut-off frequency  $f/f_{vs} < 40$ ; 5—mesh cut-off frequency; 6— $-5/3$  slope

#### 4.5 Shear-layer instability

In the context of the shear-layer instability, for a given, sufficiently long, recirculation zone length, the separated shear layer evolves in a similar manner to a mixing layer. It becomes convectively unstable due to the Kelvin Helmholtz mechanism for  $Re > 1200$ , leading to shear layer roll-up into tightly concentrated vorticity [38]. Prasad and Williamson's correlation indicates that this instability has a characteristic frequency for circular cylinders of [37]:  $f_{sL}/f_{vs} = 0.0235 \times Re^{0.67}$ . This equation shows that this is a high-frequency instability compared with the Bénard/von Kármán instability at high Reynolds numbers. The computed power spectra of the transverse velocity in the shear layer are displayed in Fig. 14. Both LES solutions had approximately the same spectral distribution. However, as discussed in the previous section, one can observe that the conventional Smagorinsky model reproduced a less dissipative power spectrum. The spectra were averaged over corresponding points along the span-wise direction. The Strouhal frequency ( $f_{vs}$ ) and its harmonics were characterized by distinct sharp peaks in the flow spectra (Fig. 14). Moreover, broadband peaks corresponding to the frequencies of shear-layer vortices  $f_{sL}$  can be observed at frequencies significantly higher the Strouhal frequency. The broadband peak at  $f_{sL}$  indicates that the shear-layer vortices occurred in a range of frequencies consistent with the DNS results of Dong et al. [6] and the experimental measurements of Prasad and Williamson [37]. The predicted frequency of the Kelvin-Helmholtz instability

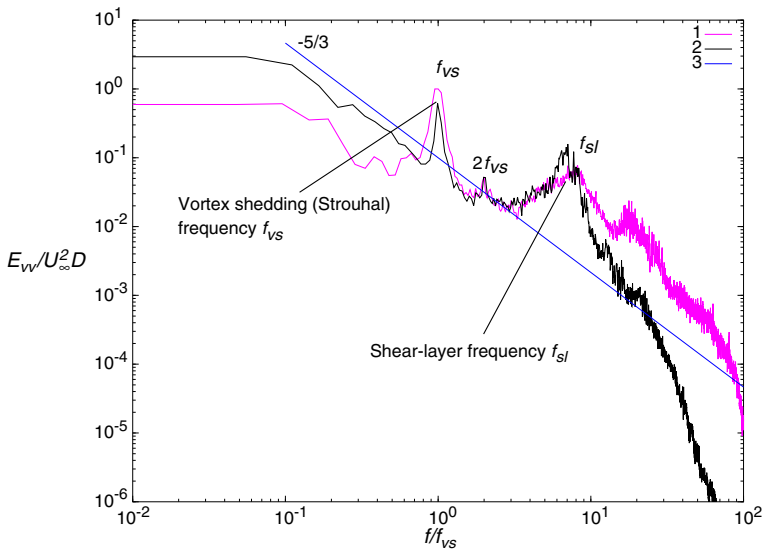


**Fig. 14** Shear-layer instability at  $Re = 3900$ . One-dimensional power spectra of the transverse velocity at the point  $x/D = 0.69$  and  $y/D = 0.69$ : 1—present LES-SMAG, 2—present LES-TKE, 3— $-5/3$  slope

by SMAG and TKE were  $f_{sL}/f_{vs} \approx 8$  and  $f_{sL}/f_{vs} \approx 7$ , respectively, which were in a good agreement with the DNS results of Dong et al. [6] ( $f_{sL}/f_{vs} = 7.83$ ) and the generalized power law approximation of Prasad and Williamson [37] ( $f_{sL}/f_{vs} = 5.99$ ).

Figure 15 shows the visualization of the instantaneous density-gradient field in a two-dimensional  $x$ – $y$  slice of the computational domain using a numerical schlieren

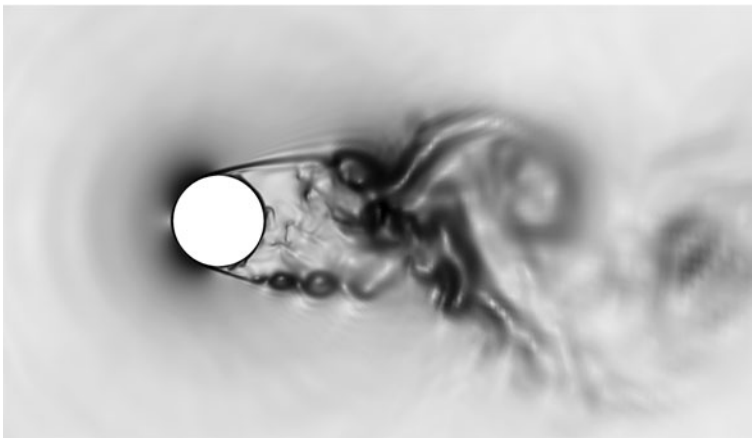


**Fig. 15** Shear-layer instability at  $Re = 3900$ . Computer visualization of the instantaneous density gradient field obtained by TKE with a numerical schlieren technique



technique. Like experimental schlieren images, the computer visualization was done according to Hadjadj and Kudryavtsev [14] using the quantity

$$S(x, y) = \beta \exp\left(-\frac{\kappa |\nabla \rho|}{|\nabla \rho|_{\max}}\right),$$

where the subscript max denotes the maximum value of the density gradient over the whole flow-field, and  $\beta$  and  $\kappa$  are two tunable parameters. The parameter  $\beta$  determines the shade of gray color that corresponds to the zero gradient and the parameter  $\kappa$  governs the amplification of small gradients. The following values were used:  $\beta = 0.975$  and  $\kappa = 15$ . In Fig. 15, well-defined vortices are clearly observed in the separating shear-layers.

#### 4.6 Discussion

One of the important issues that need to be addressed is the existence of flow bifurcation in the near wake. With respect to the experiment, the existence of the two states in the near wake is confirmed by the PIV data of Lourenco and Shih [21] and Parnaudeau et al. [35]. The first state is characterized by the presence of a U-shaped profile of the stream-wise velocity, while the second state is characterized by the presence of a V-shaped profile.

With respect to numerical simulations, both states have been found in a large number of LES and DNS studies. As noticed by Wissink and Rodi [44], the U-shaped profile appeared only in the well-resolved simulations with a span-wise size up to  $L_z = \pi \times D$ . In the LES results of Breuer [3], only U-shaped profiles were found for a span-wise size  $L_z = \pi \times D - 2\pi \times D$ . Kravchenko and Moin [19] speculated that the U shape was more likely to persist, reflecting the presence of the laminar free-shear layers. Wissink and Rodi [44] obtained the U-shape profile in their well-resolved DNS study. The DNS data provided by Wissink and Rodi [44] indicated that a U-shape profile reflects the presence of two-virtually two-dimensional-free shear layers at  $y/D \approx \pm 0.5$ , corresponding to the two detached non-turbulent boundary layers from the top and bottom of the cylinder combined with a dead air region immediately behind the cylinder. The ill-resolved shear layers resulted in V-shaped profiles due to their earlier transition, loss of coherence and more fluctuations penetrating the region behind the cylinder.

The present LES results partially confirmed the hypothesis of the influence of the shear-layer resolution on the flow bifurcation in the near wake. As discussed in Section 4.1, both states were obtained using different SGS models (Fig. 3). The conventional Smagorinsky model led to the V shape, while the dynamic  $k$ -equation model led to the U shape. This finding means that in spite of the free-shear layer grid resolution, there is sub-grid scale influence on the flow bifurcation. Another idea discussed by Wissink and Rodi [44] was the influence of the span-wise resolution. Their DNS results showed that the U-shaped state existed only for the large span-wise length ( $L_z = 8 \times D$ ). From this point of view, we can not say, whether the U-shaped solution will be obtained with the Smagorinsky model for largest span-wise lengths (e.g.  $L_z = 8 \times D$ ) or not.

In general, the present solution based on the dynamic  $k$ -equation SGS model is in fairly well agreement with the DNS data of Wissink and Rodi [44], which may be considered as a reference solution for this benchmark case. At the same time, the

conventional Smagorinsky model is based on the assumption of the local equilibrium of the SGS kinetic energy, which may lead to the fastest transition. However, the possibility of the flow bifurcation should be taken into account. More important is that this bifurcation is confirmed by the experimental data. With respect to DNS, the U-shaped solution is more likely. With respect to the experiment, we do not know which state is more likely or stable, etc. Thus, in the authors' opinion, some analysis with application of stability theory should be done to provide more insight.

Table 2 incorporates integral flow parameters collected from available experimental and numerical (DNS and LES) results. All flow features such as thin laminar boundary layers, unsteady separation, wake dynamics and shear-layer instability were captured well in the present numerical simulation. In this paper the 'classical, O-type mesh was utilized for the flow modeling. The resolution of the mesh was chosen to achieve a 'top' level  $300 \times 300 \times 64$  mesh size compared to those available in published LES literature (Table 1). Since the goal was to assess the LES capabilities implemented in OpenFOAM, only two runs were carried out.

A mesh independence study was not conducted since large-eddy simulations are still computationally very expensive. Moreover, as reported at the last Parallel CFD '11 conference, DNS/LES calculations will still be expensive in the near future. This is due to several reasons [25]: Firstly, processor clock-rate is not increasing due to the technology limit (heat generation is proportional to clock-rate in cube power). Secondly, on one hand, significant speedup (by orders of magnitude) may be achieved only via massive parallelism. On the other hand, MPI communication is another limit, and it is considered as the lowest limit. When the processor/resolution ratio is increased, the time required for MPI communication between computational nodes will also increase. The best-in-class solvers demonstrate perfect scaling with a number of grid nodes  $N_p > 10^5$  per one core. Of course, this cut-off number depends on a MPI/memory speed ratio. Typically, the state-of-the-art HPC systems provide computation time for one time step with  $N_p = 10^5$  about 0.75–7.50 s, and this number will not change significantly due to the aforementioned factors. This finding means that LES/DNS runs will take a long time. For example, turbulent flows with  $Re = 10^6 - 10^7$  will require approximately  $10^7$  time steps. We make an assumption that for turbulent flows with vortex propagation, the number of time steps may be proportional to the Reynolds number. Assuming that one time step lasts 1 s, the total calculation time will take 2777 h or 115 days. Concluding, there are two limits which determine the overall performance: execution time (time per one step per one grid point, which is actually fixed now because the processor clock-rate is not increasing) and the number of useful MPI nodes, that depends on a problem size and network communication rate. Corollary, LES/DNS runs will remain expensive. Especially for simulations of turbulent flows where a large number of grid points ( $> 10^9$ ) and large number of time steps ( $> 10^5$ ) are required.

With respect to the numerics, a second-order FVM with central-difference schemes was adopted, which is commonly used in industry. Such schemes do not exhibit numerical dissipation and there is no spurious damping of the high frequencies. However, the disadvantage of using such schemes is the dominance of the dispersive error, which makes them sensitive to such aspects as grid discontinuities and outflow boundary conditions [30]. Furthermore, well-posed turbulent inlet boundary conditions are important in any practical LES. However, this is not focused upon in this paper due to the limitations of the mesh applied (as discussed in Section 2). Finally,

**Table 2** Overview of the experimental and LES works of the circular cylinder flow at  $Re = 3900$ : parameters and integral flow features

Contributors	Method	$N_{vp}$	M	$\langle C_d \rangle$	$\langle C_l \rangle_{rms}$	St	$-\langle C_{p,b} \rangle$	$\langle L_T \rangle / D$	$-\frac{\langle u_{min} \rangle}{U_\infty}$	$\langle \theta_{sep} \rangle$
Cardell [4] (from [29])	HWA					0.215		1.33	0.25	
Lourenco and Shih [21]	PIV			0.99		0.22		1.19	0.24	86°
Norberg [31, 32]	HWA			0.98			0.90			
Ong and Wallace [33]	HWA				0.04–0.15					
Ma et al., Case II [26]	DNS	131		0.84		0.21		1.59		
Dong et al. [6]	PIV					0.22		1.36–1.47	0.252	
Dong et al. [6]	DNS	40–50				0.20		1.41–1.59	0.291	
Parnaudeau et al. [35]	PIV					0.21		1.51	0.34	
Wissink and Rodi, Case E [44]	DNS	10				0.22		1.588	0.33	87°
Mittal and Moin [30]	LES	12		1.00		0.21	0.93		0.35	87°
Breuer, Case D3 [3]	LES	22/44		1.02		0.22	0.94	1.37	0.23	87°
Kravchenko and Moin [19]	LES	7		1.04		0.21	0.94	1.35	0.37	88°
Franke and Frank [7]	LES	42	0.2	0.99		0.21	0.85	1.64		88°
Alkishiwi et al. [1]	LES	37	0.05	1.05		0.22		1.31	0.28	
Parnaudeau et al. [35]	LES	52				0.21		1.56	0.26	
Mani et al. [27]	LES	60	0.2	0.99		0.21	0.86		0.33	86°
Meyer et al. [28]	LES	60		1.07		0.22	1.05	1.18	0.26	89°
Meyer et al. [28]	LES	60		1.05		0.21	0.92	1.38	0.35	88°
Ouvrard et al. [34]	LES		0.1	0.94	0.092	0.22	0.83	1.56		
Wornom et al. [45]	LES	30	0.1	0.99	0.11	0.21	0.88	1.45		89°
Present	SMAG	150	0.2	1.18	0.44	0.19	0.8	0.9	0.26	89°
	TKE	150	0.2	0.97	0.09	0.209	0.91	1.67	0.27	88°

non-reflecting boundary conditions were utilized and tested to prevent spurious non-physical reflections from entering the computational domain.

## 5 Concluding Remarks

The objective of the present work was an extensive investigation of the numerical aspects influencing the quality of LES solutions, implemented in the OpenFOAM toolbox. With this purpose, the flow past a circular cylinder at a sub-critical Reynolds number of 3900 and Mach number of 0.2 was simulated using an LES technique with the dynamic  $k$ -equation SGS model. To check SGS influence, an additional run was carried out with the conventional Smagorinsky model. Particular attention was put on the statistical convergence. To achieve fully converged data in the present LES, the statistics were collected for a time interval of about 150 vortex shedding periods.

Predicted integral flow parameters, local first-order statistics and one-dimensional energy spectra were analyzed in detail and compared with existing experimental data. In general, the LES results agreed fairly well with the experimental data of Norberg [31], Lourenco and Shih [21], Prasad and Williamson [37], Ong and Wallace [33] and Parnaudeau et al. [35], as well as with DNS studies [6, 26, 44]. These comparisons gave an indication of the adequacy and the accuracy of the OpenFOAM toolbox for prediction of turbulent separated flows using large-eddy simulation.

Analysis of the available experimental data, DNS data and LES data revealed the existence of the flow bifurcation (the U-shaped and V-shaped states) for this benchmark case. Recently, Wissink and Rodi [44] performed a DNS study using extremely-high mesh resolution for the flow over a circular cylinder at  $Re = 3300$  and concluded that a U-shaped solution was more likely. This finding was confirmed partially by the present results: the solution based on the dynamic  $k$ -equation SGS model converged to the U-shaped state, while the conventional Smagorinsky model converged to the V-shaped state. However, both flow states have been identified experimentally (Lourenco and Shih [21] and Parnaudeau et al. [35]).

**Acknowledgements** This work was conducted as a part of the CenBio Center for environmentally-friendly energy. We are very thanked for the uninterrupted HPC computational resources and the useful technical support provided by the Norwegian Meta center for Computational Science (NOTUR). We would also like to thank the reviewers for very useful suggestions and comments to this work.

## References

1. Alkishriwi, N., Meinke, M., Schröder, W.: A large-eddy simulation method for low Mach number flows using preconditioning and multigrid. *J. Comput. Fluids*. **35**, 1126–1136 (2006)
2. Beaudan, P., Moin, P.: Numerical experiments on the flow past a circular cylinder at sub-critical Reynolds number. Technical Report TF-62, CTR Annual Research Briefs, NASA Ames/Stanford University (1994)
3. Breuer, M.: Large eddy simulation of the sub-critical flow past a circular cylinder: numerical and modeling aspects. *Int. J. Numer. Methods Fluids* **28**, 1281–1302 (1998)
4. Cardell, G.S.: Flow past a circular cylinder with permeable splitter plate. Data taken from Mittal [29] (1993)
5. Chorin, A.: Numerical solution of Navier-Stokes equations. *Math. Comput.* **22**, 745–762 (1968)

6. Dong, S., Karniadakis, G.E., Ekmekci, A., Rockwell, D.: A combined direct numerical simulation particle image velocimetry study of the turbulent air wake. *J. Fluid Mech.* **569**, 185–207 (2006)
7. Franke, J., Frank, W.: Large eddy simulation of the flow past a circular cylinder at  $Re = 3900$ . *J. Wind Eng. Ind. Aerod.* **90**, 1191–1206 (2002)
8. Fureby, C.: Towards the use of large eddy simulation in engineering. *Prog. Aerosp. Sci.* **44**, 381–396 (2008)
9. Fureby, C.: On subgrid scale modeling in large eddy simulations of compressible fluid flow. *Phys. Fluids* **8**(5), 1301–1311 (1996)
10. Fureby, C., Tabor, G., Weller, H.G., Gosman, A.D.: A comparative study of subgrid scale models in homogeneous isotropic turbulence. *Phys. Fluids* **9**(5), 1416–1429 (1997)
11. Garnier, E., Adams, N., Sagaut, P.: *Large Eddy Simulation for Compressible Flows*. Springer, New York (2009)
12. Germano, M., Piomelli, U., Moin, P., Cabot, W.: A dynamic subgrid-scale eddy viscosity model. *Phys. Fluids* **3**(7), 1760–1765 (1991)
13. Geurts, B.: *Elements of Direct and Large-Eddy Simulation*. R.T. Edwards, Philadelphia (2004)
14. Hadjadj, A., Kudryavtsev, A.: Computation and flow visualization in high-speed aerodynamics. *J. Turbul.* **6**(16), 33–81 (2005)
15. Hestens, M., Steifel, E.: Methods of conjugate gradients for solving systems of algebraic equations. *J. Res. Natl. Bur. Stand* **29**, 409–436 (1952)
16. Issa, R.: Solution of the implicitly discretized fluid flow equations by operator splitting. *J. Comput. Phys.* **62**, 40–65 (1986)
17. Jacobs, D.: Preconditioned conjugate gradient methods for solving systems of algebraic equations. Tech. rep., Central Electricity Research Laboratories, Leatherhead, Surrey, England (1980)
18. Jeong, J., Hussain, F.: On the identification of a vortex. *J. Fluid Mech.* **285**, 69–94 (1995)
19. Kravchenko, A., Moin, P.: Numerical studies of flow over a circular cylinder at  $Re=3900$ . *Phys. Fluids* **12**(2), 403–417 (2000)
20. Lilly, D.K.: A proposed modification of the Germano subgrid-scale closure method. *Phys. Fluids* **4**(3), 633–635 (1992)
21. Lourenco, L.M., Shih, C.: Characteristics of the plane turbulent near wake of a circular cylinder, a particle image velocimetry study. Published in Ref. [2] (1993)
22. Lysenko, D.A., Ertesvåg, I.S., Rian K.E.: Testing of OpenFOAM CFD code for plane turbulent bluff body flows within conventional URANS approach. In: *Proceedings, 8th Int. Conf. on CFD in Oil and Gas, Metallurgical and Process Industries*. Trondheim (2011)
23. Lysenko, D.A., Ertesvåg, I.S., Rian, K.E.: Turbulent bluff body flows modeling using OpenFOAM technology. In: Skallerud, B., Andersson, H.I. (eds.) *MekIT'11-Sixth National Conference on Computational Mechanics*, pp. 189–208. Trondheim (2011)
24. Lysenko, D.A., Ertesvåg, I.S., Rian K.E.: Modeling of turbulent separated flows using OpenFOAM. *Comput. Fluids* (2012). doi:[10.1016/j.compfluid.2012.01.015](https://doi.org/10.1016/j.compfluid.2012.01.015)
25. Löhner, R.: Increasing the number of cores for industrial/legacy codes: approaches, implementation and timings. In: *Proceedings, 23rd, Int. Conf. on Parallel Computational Fluid Dynamics, ParCFD 2011*. Barcelona (2011)
26. Ma, X., Karamanos, G.S., Karniadakis, G.E.: Dynamics and low-dimensionality of a turbulent near wake. *J. Fluid Mech.* **410**, 29–65 (2000)
27. Mani, A., Moin, P., Wang, M.: Computational study of optical distortions by separated shear layers and turbulent wakes. *J. Fluid Mech.* **625**, 273–298 (2009)
28. Meyer, M., Hickel, S., Adams, N.A.: Assessment of implicit large-eddy simulation with a conservative immersed interface method for turbulent cylinder flow. *Int. J. Heat Fluid Flow* **31**, 368–377 (2010)
29. Mittal, R.: Progress on LES of flow past a circular cylinder. In: *Annual Research Briefs, Center of Turbulence Research*, pp. 233–241. Stanford University (1996)
30. Mittal, R., Moin, P.: Suitability of upwind biased schemes for large-eddy simulation. *AIAA J.* **30**(8), 1415–1417 (1997)
31. Norberg, C.: Experimental investigation of the flow around a circular cylinder: influence of aspect ratio. *J. Fluid Mech.* **258**, 287–316 (1994)
32. Norberg, C.: Flow around a circular cylinder: aspects of fluctuating lift. *J. Fluids Struct.* **15**, 459–469 (2001)
33. Ong, L., Wallace, J.: The velocity field of the turbulent very near wake of a circular cylinder. *Exp. Fluids* **20**, 441–453 (1996)

34. Ouvrard, H., Koobus, B., Dervieux, A., Salvetti, M.V.: Classical and variational multiscale LES of the flow around a circular cylinder on unstructured grids. *Comput. Fluids* **39**, 1083–1094 (2010)
35. Parnaudeau, P., Carlier, J., Heitz, D., Lamballais, E.: Experimental and numerical studies of the flow over a circular cylinder at Reynolds number 3900. *Phys. Fluids* **20**(8), 085101 (2008)
36. Poinso, T., Lele, S.: Boundary conditions for direct simulations of compressible viscous flows. *J. Comput. Phys.* **101**, 104–129 (1992)
37. Prasad A., Williamson, C.H.K.: The instability of the shear layer separating from a bluff body. *J. Fluid Mech.* **333**, 375–402 (1997)
38. Shanbhogue, S.J., Husain, S., Lieuwen, T.: Lean blowoff of bluff body stabilized flames: scaling and dynamics. *Prog. Energy Combust. Sci.* **35**, 98–120 (2009)
39. Smagorinsky, J.S.: General circulation experiments with primitive equations. *Mon. Weather Rev.* **91**(3), 99–164 (1963)
40. Son, J., Hanratty, T.: Velocity gradients at the wall for flow around a cylinder at Reynolds numbers from  $5 \times 10^3$  to  $10^5$ . *J. Fluid Mech.* **35**, 353–368 (1969)
41. Vreman, A.W., Geurts, B.J., Kuerten, J.G.M.: Subgrid-modelling in LES of compressible flow. *Appl. Sci. Res.* **54**, 191–203 (1995)
42. Welch, P.: The use of fast Fourier transform for the estimation of power spectra: a method based on time averaging over short, modified periodograms. *IEEE Trans. Audio Electroacoust.* **15**(6), 70–73 (1967)
43. Weller, H.G., Tabor, G., Jasak, H., Fureby, C.: A tensorial approach to computational continuum mechanics using object-oriented techniques. *Comput. Phys.* **12**(6), 620–631 (1998)
44. Wissink, J.G., Rodi, W.: Numerical study of the near wake of a circular cylinder. *Int. J. Heat Fluid Flow* **29**, 1060–1070 (2008)
45. Wornom, S., Ouvrard, H., Salvetti, M.V., Koobus, B., Dervieux, A.: Variational multiscale large-eddy simulations of the flow past a circular cylinder: Reynolds number effects. *Comput. Fluids* **47**(1), 44–50 (2011)